Analysis of the aerogel threshold Cerenkov data from AMS flight (STS-91)

F. Barao, J. Favier, F. Mayet, G. Barreira, M. Buenerd, G. Castellini, E. Choumilov, A. Gougas, R. Kossakowski, G. Laurenti, et al.

AMSnote-99_38
ISN 99.84
LAPP-EXP-99.06
November 3rd, 1999

Analysis of the Aerogel Threshold Čerenkov data from AMS flight (STS-91)

F. Barao[1,3], J. Favier[1], F. Mayet[2]
G. Barreira[3], M. Buenerd[2], G. Castellini[6], E. Choumilov[5],
A. Gougas[4], R. Kossakowski[1], G. Laurenti[7], S-C. Lee[4],
Y-T. Oyang[4], V. Plyaskine[5], D. Santos[2], V. Pojidaev[5], J.P. Vialle[1]

[1] Laboratoire d'Annecy-le-Vieux de Physique des Particules (IN2P3-CNRS)
F-74941 Annecy-le-Vieux cedex, France

[2] Institut des Sciences Nucléaires (IN2P3-CNRS)
53, Avenue des Martyrs, 38026 Grenoble cedex, France

[3] Laboratório de Instrumentação e Física Experimental de Partículas.
Avenida Elias Garcia, 14-1., 1000 Lisboa, Portugal

[4] Institute of Physics-Academia Sinica
Taipei 115, Taiwan, Republic of China

[5] Institute of Theoretical and Experimental Physics
B. Cheremushkinskaya Ul, Moscow, Russian Federation

[6] INFN Sezione di Firenze
Largo E. Fermi 2, I - 50125 Firenze, Italy

[7] University of Bologna - INFN Sezione di Bologna
Via Irnerio,46 , I - 40126 Bologna ,Italy

Abstract

The Alpha Magnetic Spectrometer (AMS), in a preliminary version (phase 1), was flown in June 1998 on a 51.6° inclinated orbit and at an altitude of 370 km, on board of the space shuttle Discovery. This flight has allowed to measure the fluxes of several particles ($e^{\pm}$, $p^{\pm}$, He). AMS includes an Aerogel Threshold Čerenkov detector (ATC) to separate $\bar{p}$ from e^- background, for momenta below 3.5 GeV/c. This note includes a short description of the ATC and reports on its performances during STS-91 flight.

LABORATOIRE D'ANNECY-LE-VIEUX DE PHYSIQUE DES PARTICULES
IN2P3/CNRS - UNIVERSITÉ DE SAVOIE
Chemin de Bellevue - B.P. 110 - F 74941 Annecy-le-Vieux Cedex - Tél. 04 50 09 16 00 - Telecopie 04 50 27 94 95

1 Introduction

The first phase of the AMS experiment (AMS-01) was achieved on board of the space shuttle Discovery, during 10 days in June 1998. The main objective was to test the spectrometer's behaviour in orbit, in order to prepare a phase in which the experiment will take place on the International Space Station (ISS) for several years. During the shuttle flight, 100 million events have been recorded, allowing the fluxes of several particle species ($e^{\pm}$, $p^{\pm}$, He) to be measured [1].
The AMS-01 detector was composed of a permanent magnet, a Time-of-Flight counter (TOF), a silicon tracker (TRK), anticoincidence (veto)counters (ACC) and an Aerogel Threshold Čerenkov counter (ATC).
This note provides a short description of the ATC and reports on its performances through the flight data analysis.

1.1 Role of ATC in AMS

One of the purposes of the AMS Shuttle flight was to search for cosmic antiprotons and to measure $\bar{p}/p$ ratio for momenta below 3.5 GeV/c (the ATC momentum threshold).
The major background component to the $\bar{p}$ sample is expected to come from misidentified electrons and the signal to background ratio is estimated to be : $\bar{p}/e^- \sim 10^{-2}$ for the considered P range.
While TOF counters [2] ($\Delta\beta/\beta \simeq 3.3\%$) allow to separate $\bar{p}$ and e^- below 1.5-2 GeV/c (fig. 4), ATC extends this discrimination range to 3.5 GeV/c. Therefore, $\bar{p}/e^-$ separation can profit from ATC redundancy up to 1.5-2 GeV/c and relies essentially on the ATC up to 3.5 GeV/c.
Positrons are also an important issue for AMS-01, for which protons constitute the dominant background, with a typical rate : $p/e^+ \sim 10^3$. Although the ATC design was not optimized for these particles, positron separation can be improved by using appropriate ATC cuts.

1.2 Physical principle of the ATC

Many balloon-borne experiments [3] have included a Čerenkov counter and a Ring Imaging Čerenkov counter is under study for the next phase of the AMS experiment [5].
The ATC counter, used in AMS-01, profits from Čerenkov effect to separate $\bar{p}$ from e^- at low energy.
The number of photons created by Čerenkov effect, in a material of refractive index n, is given by:

$$N_{pe} \propto L_{aero} \times Z^2 \times sin^2\theta = L_{aero} \times Z^2 \times (1 - \frac{1}{n^2\beta^2}) \quad (1)$$

where L_{aero} is the path length in the material, θ is the Čerenkov angle and Z the charge of the incoming particle.
This leads to the following threshold values (in beta or momentum) :

$$\beta_{thres} = 1/n \ ; \ P_{thres} = \frac{mc}{\sqrt{n^2 - 1}} \quad (2)$$

where m is the rest mass of the particle.
The aerogel material ($n = 1.035 \pm 0.001$) has been chosen so that its refractive index

was as low as possible, giving β_{thres} close to 1, while giving a sufficient number of photo-electrons[1].
The corresponding thresholds, for several particle species, are given in the following table.

Particle	$e^{\pm}$	$\pi^{\pm}$	p ($\bar{p}$)	He (He)
P_{thres}	1.91 MeV/c	0.52 GeV/c	3.51 GeV/c	14.0 GeV/c

In the 0.5-3.5 GeV/c range, $e^{\pm}$ are far above their threshold, thus giving a full amplitude signal in ATC, whereas, in principle, p and $\bar{p}$ of momentum less than 3.5 GeV/c, are not expected to give any signal, thus leading to $\bar{p}/e^{-}$ separation.

2 ATC Design

The elementary component of the ATC detector is the aerogel cell ($11 \times 11 \times 8.8\ cm^3$, see figure 2), filled with eight 1.1 cm thick aerogel blocks. The emitted photons are reflected by three 250 μm teflon layers surrounding the aerogel blocks, until they reach the photomultiplier's window (Hamamatsu R-5900).
The ATC detector is made of 168 cells arranged in 2 layers (80 cells in the upper one and 88 cells in the lower one). The 2 layers are shifted (fig. 1 and 3) in order to minimize the loss of tracks passing in between the cells.

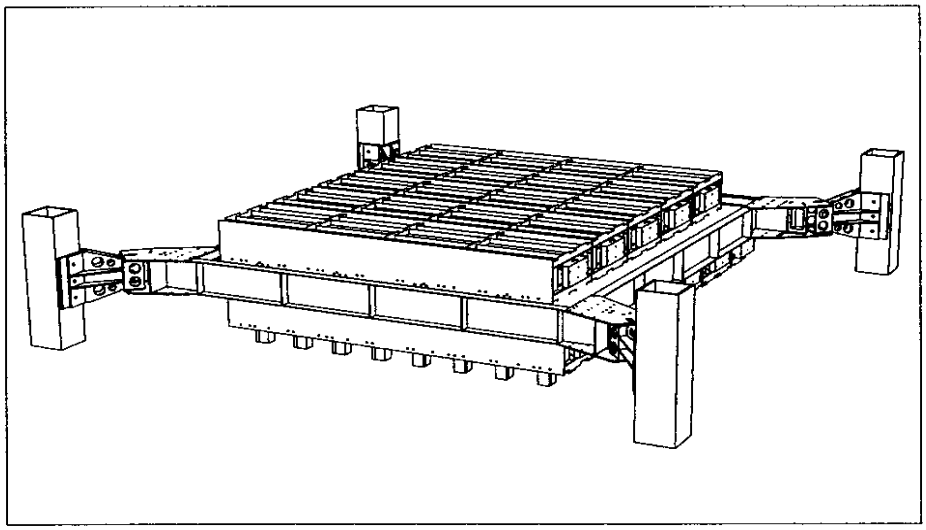

Figure 1: ATC detector design. The 2 shifted layers (in x and y directions) can be seen together with the structure which allows to mount the ATC directly on the USS.

The limiting processes to the Čerenkov photon detection are the Rayleigh scattering ($L_R \propto \lambda_\gamma^4$) and the absorption ($L_{abs} \propto \lambda_\gamma^2$). This two effects are decreasing with increasing photon wavelength. For this purpose, a wavelength shifter is used and placed in the

[1]During R&D, the achieved value was : $n_{p.e} \geq 7$ per cell

middle of each cell (see fig.2). It consists of a thin layer of tedlar (25 μm) soaked in a PMP solution (1-Phenyl-3-Mesityl-2-Pyrazolin) and placed into a polyethylene envelope (50 μm), to avoid contact between PMP and the aerogel material. This allows to shift wavelength from $300nm$ up to $420nm$. It should be noticed that maximum efficiency of the R-5900 photomultiplier tube [6] is at $\lambda \sim 420nm$.
The use of the shifter leads to an overall increase in number of p.e, estimated to be $\sim 40.\%$.

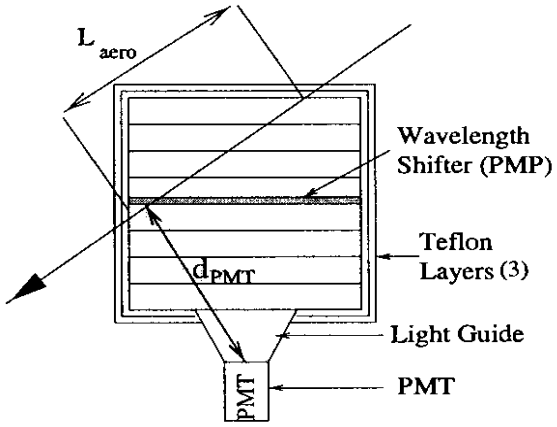

Figure 2: The aerogel cell. The 8 blocks of aerogel are shown together with 3 teflon layers and the PMP wavelength shifter laying in the middle of the cell. The parameters L_{aero} and d_{PMT}, used in the ATC analysis, will be defined in section 3.

Two diagonal consecutive cells are coupled into one electronic channel. The same readout electronics as for the TOF counter is used for the ATC, optimized for the lower input charge level provided by the ATC. The 168 signals are fed into 84 front-end cards directly on the module. This front-end cards convert the charge in a signal whose time length depends on the logarithm of the charge.
This time is digitized by the TDC cards (SFEC) placed in the general crate assembly.
One module of 16 cells is powered by two HV units (for redundancy), located on the 2 edges of the ATC.

3 Flight Data Analysis

3.1 ATC Calibration

The goal of the ATC calibration is to provide, for each cell, the coefficients of the expression relating the number of photo-electrons to the time measurement provided by the SFEC cards. We recall that for measuring charges, we were imposed by the AMS time schedule to use an electronics scheme convenient for the TOF, but not suited to our goal : the charge is converted in time in the front-end electronics; this has for consequences to pollute the original charge signal by any after-pulses coming during the integration time (typically 200 nsec).

The formula used to describe the electronics behaviour is an approximation not correct for large dynamics, but sufficiently accurate for operating at few numbers of photo-electrons as it was expected for ATC. It involves the PMT gains (very dispersed) and the electronics characteristics:

$$Q_e(i) = A \times g(i) \times (e^{\frac{t+C_2(j)}{C_3}} + C_1) \quad (3)$$

$Q_e(i)$: detected charge in photo-electron unit
A: overall normalization factor (equal for the 168 cells)
g(i): relative gain (average=1.) for each PMT i
C_3 : parameter governing the logarithmic behaviour of the front-end electronics
$C_2(j)$: time "pedestals", relative to each electronic channels j
C_1=0.

The coefficients C_3 of the exponential could not be correctly measured card by card before the ATC mounting because their values depend strongly of the final ATC cabling and PMT's input capacitances on the amplifiers. Measurements on the ATC after the flight have shown that they were all equal within ±2.% to the value 220.
The C_2 coefficients are taken from the raw data time distributions. A preliminary version of calibration coefficients has been provided before STS-91 flight using a single p.e calibration made in Zurich (see fig.5). The final coefficients were obtained, as foreseen, from the flight data themselves, which is indeed the safest way. Selecting below threshold protons provides automatically, and with high statistics, a peak at one p.e (coming from the residual scintillation light of 0.5 p.e in average per cell). Difficulties came from the fact that 25.-30.% of the R-5900 PMT's were not giving a nice single p.e distribution. Nevertheless, the high number of recorded protons has permitted to equalize the 168 gains, as it can be seen in fig.6.
As described below, the ATC luminosity (number of p.e for $\beta = 1.$) is obtained using high β protons from STS-91 flight. AMS data available on the ntuples are calibrated, and the numbers available are already in photo-electron.

3.1.1 Front-end electronics thresholds

The front-end electronics has, by principle, a threshold. Although they were tested to be very similar from channel to channel (dispersion below 10.%), the differences of PMT gains induced a dispersion over the thresholds calculated in photo-electron units. Fig.7 shows the distribution of the 168 thresholds. The mean value is seen to be 0.37 p.e. This threshold has to be taken into account for extracting, from the number of 0 of the Poisson distribution, an estimation of the number of p.e for $\beta = 1$. The correction is 15.% in average.

3.2 Detector Performance

In this section, the ATC performances during STS-91 flight will be discussed.
This will concern :

- The global number of photo-electrons reached by the ATC at $\beta = 1$.
- The dependence of the pathlength in aerogel and the particle's charge on $n_{p.e}$.
- The dependence of the impact parameter (closest distance to PMT) on $n_{p.e}$.
- ATC Monitoring
- Cross-check of the aerogel refractive index

3.2.1 The ATC absolute number of photo-electrons ($n_{p.e}$) for $\beta = 1$ particles.

There are several methods to evaluate $n_{p.e}$ in each cell crossed by a $\beta = 1$ particle, which is the basic number entering in ATC rejection ability. One is to use calibration (i.e mean number of charges for one p.e distribution). It consists of dividing the mean value of the charge distribution obtained using selected tracks (for geometry and $\beta = 1.$) by this calibration.
This method is not accurate since the calibration procedure is affected by important errors (20 %) and also the after-pulses problems encountered with our PMTs introduce non-linearities and large variances on the charge distributions. This also discards the other method using the relation : $n_{p.e}$=<N>$^2/Var(N)^2$, where <N> and Var(N) are respectively the mean value and the variance of the distribution.
The best method, in our case, and also the one which is the closest to the use of ATC, consists in comparing the number of "no signals" in the cell with the number expected by the Poisson distribution for a given average $n_{p.e}$. It has been done with the high energy part of the STS-91 protons data. This requires three conditions:

- β has to be equal to 1. But if we select $P \geq 15$ GeV/c ($\beta \geq 0.99$) it is easy to correct $n_{p.e}$ knowing the proton spectrum.
- It must be ensured that the track used is really crossing the aerogel material of the cells, which means a good selection on track qualities and geometry knowledge.
- The charge threshold of the electronics must also be taken into account (see above in sec. 3.1); if not the $n_{p.e}$ is under-evaluated.

Using the following cuts and averaging on all cells except those listed below (see sec. 3.2.3), we obtained :

$$n_{p.e} = 2.9 \text{ , for the upper plane}$$

$$n_{p.e} = 3.3 \text{ , for the lower plane}$$

These values, after correcting for electronic thresholds and the average β effect of the protons sample, become :

$$n_{p.e} = 3.51 \pm 0.02 \text{ , for the upper plane}$$

$$n_{p.e} = 4.02 \pm 0.02 \text{ , for the lower plane}$$

3.2.2 ATC ageing

The ATC has suffered a fast degradation with time : the average $n_{p.e}$ by cell (for $\beta = 1$) was about 5 p.e/cell in November 97. During the flight, this value decreased to 3.1 p.e/cell and at the November 98 CERN test beam, it reached 1.5 p.e/cell which corresponds to life time of about 300 days. During the same period, a reference cell at room temperature has decreased with a much larger life time of 1044 days[2].

3.2.3 ATC Monitoring

During STS-91 flight, the online monitoring has shown that a few number of cells were not working properly. This has been confirmed by the offline analysis.
The following table indicates, amongst the 168 cells of the detector, for a given period of time, the cells that were found to have an inefficiency greater than 15%. L5 indicates the module L5. Origin of time is taken from the first event observed in AMS. One should add to these cells, cells 168 and 166, corresponding to the electronic channel 84, which did not work for the whole flight.

Period (hours)	Run Times	Layer 1	Layer 2
0-20	98/06/03 19:00 - 98/06/04 15:00	11,68	103,133,L5
20-80	98/06/04 15:00 - 98/06/07 03:00	11,68	93,103,133,L5
80-209	98/06/07 03:00 - 98/06/12 12:00	11,68	93,103,133

It can be observed that inefficient cells are mainly located at the very edge of the ATC geometrical acceptance. Thus, the ATC geometrical efficiency is not decreased too much by this effect ($\epsilon_{(geo+cells)}/\epsilon_{geo} \simeq 0.93$).

3.2.4 Dependence of $n_{p.e}$ with L_{aero} and Z

As inferred from eq.1, the number of Čerenkov photons is expected to be proportional to the path length acrossed by the particle in the aerogel cell.
Figure 8 shows the number of photo-electrons as a function of path length in aerogel (L_{aero}), for $\beta \sim 1$ particles.
It shows that the ATC linear response is consistent with expectations, within the statistical uncertainties.

The number of photo-electrons is also proportional (eq.1) to the square of the particle's charge.
Figure 9 shows Number of photo-electrons as a function of P(GeV/c), for particles identified as helium by AMS (upper part) and protons (lower part).
Above threshold, the number of p.e follows the expected dependence.

$$n_{p.e} \propto (1 + m^2/P^2) \tag{4}$$

[2]We have not yet dismounted a module for evaluation, but we suspect the solvent of the black RTV (abundantly used for light tightness) to be responsible for this effect.

Far above threshold, where particles give a full signal in ATC, $\frac{n_{p.e}(He)}{n_{p.e}(p)}$ ratio is in good agreement with the expected factor 4.

3.2.5 Residual light

For low momentum (below threshold), the residual light (see fig. 9) can be evaluated to be $\sim 1p.e$ for protons, summed over the 2 ATC layers. This is due to δ-rays, Čerenkov effect in the wavelength shifter component and scintillation. Below $\sim 1.$ GeV/c an increase in residual light, due to scintillation, is observed (see detailed view in fig. 9). The residual light is also slightly increasing between 1 GeV/c and 3 GeV/c (see fig. 9). This may be explained by δ-rays, and Čerenkov effect in the polyethylene and teflon layers (we estimate the threshold for Čerenkov effect in these materials to be $\sim 1.$ GeV/c . At 2.7 GeV/c , the $n_{p.e}$ will be 10 % of the maximum value). This effect will cause the proton rejection (for e^+ selection) to decrease between 1 GeV/c and 3 GeV/c (see fig. 16).

3.2.6 Distance to PMT

The closest distance of the track to the center of the PMT window (see figure 2), is defined as the impact parameter (d_{PMT}) and it turns out that this variable is strongly correlated with the cell signal.
In fact, the number of collected photo-electrons ($n_{p.e}$) is expected to increase with decreasing impact parameter, for several reasons:

- The probability of photons entering directly in the PMT window (without any reflections) is increased, which limits the losses due to following reflections.
- The path length of photons in aerogel will be shorter in average leading to less absorption.
- For very low impact parameter ($d_{PMT} \leq 1cm$), the particle is expected to produce a large number of photons from Čerenkov effect in the PMT window.

Figure 10 shows the number of p.e ($n_{p.e}$) as a function of the impact parameter distance squared.
The signal enhancement for low impact parameter is clearly visible and is estimated to be $\sim 6p.e$ per layer.

3.2.7 Refractive Index Evaluation

Using STS-91 flight data, it is possible to evaluate the refractive index of the aerogel.
As shown in equation 1, $n_{p.e} \propto (1 - \frac{1}{n^2\beta^2})$. Hence above threshold $n_{p.e}$ is expected to be a linear function of $1/\beta^2$.
Figure 11 shows the number of p.e as a function of $1/\beta^2$, for the second ATC layer
Using the extrapolation of the background (residual light), one can extrapolate the observed threshold and thus evaluate the value of n.

$$n^2 = 1/\beta^2_{thre} \simeq 1.07 \rightarrow n \simeq 1.0344 \tag{5}$$

Neglecting index dispersion, this value is in good agreement with the refractive index measured at LAPP[3] ($n = 1.0356 \pm 0.001$) and the value given by the manufacturer [7] (n=1.035).

3.3 $\bar{p}/e^-$ discrimination

The discrimination of $\bar{p}$ from e^- background is obtained by imposing first that the particle must cross the 2 ATC layers, leading to an overall geometrical efficiency of 72%. The second condition is that the particle does not produce any signal in ATC, this leads to antiproton detection efficiency ($\epsilon_{\bar{p}}$) and electron rejection (R_{e^-}) as discussed below.
In order to estimate $\epsilon_{\bar{p}}$ and R_{e^-} , two control samples are being used. Above threshold particles (high energy protons near equator, with P $\geq$ 15 GeV/c and $\beta \geq 0.99$) will have the same behaviour as electrons. A sample of below threshold particles (protons with low β) is used to evaluate antiprotons behaviour in ATC.
Figure 12 and 13 show distributions of $n_{p.e}$ for particles above and below threshold.

On figure 14, ATC rejection is presented as a function of magnetic latitude (θ_{mag}).
It can be said that the rejection is better near the equator, indicating that the sample of high energy particles is less contaminated by badly reconstructed tracks. In fact the geomagnetic cutoff [8] prevents from having low energy particles. Thus we take advantage of the magnetic cutoff to select a pure sample of high energy particles, by imposing $\theta_{mag} \leq 0.5$, where θ_{mag} is the magnetic latitude evaluated with a shifted dipole model.
As shown in figure 12, most of above threshold particles give $\sim$ 6 p.e (summed over the 2 ATC layers). A tail of higher number of p.e, due to after-pulses in the PMT, can be observed. On the other hand, a few percentage of e^- lead to a low signal in ATC. This is due to statistical fluctuations and is related to the e^- rejection.
For a given cut on p.e number, the e^- rejection (R_{e^-}) is defined as :

$$R_{e^-}(n_{cut}) = \mathcal{N}_{e^-}/\mathcal{N}_{e^-}(n_{p.e} \leq n_{cut}) \tag{6}$$

Below threshold particles are selected as protons of momentum less than 3.5 GeV/c and β less than 0.97. It can be noticed on fig. 13 that most of the protons do not give any signal. The residual light effect can be observed around 1 p.e with a tail produced by $\delta-$rays, scintillation and after pulses. For a given cut on p.e number, the $\bar{p}$ efficiency is defined as :

$$\epsilon_{\bar{p}}(n_{cut}) = \mathcal{N}_{\bar{p}}(n_{p.e} \leq n_{cut})/\mathcal{N}_{\bar{p}} \tag{7}$$

Figure 15 shows the antiproton efficiency as a function of P(GeV/c) for different cuts on $n_{p.e}$. The electron rejection (R_{e^-}) is also shown for each cut. Based on figure 7, which shows distribution of electronic triggers, an ATC cut can be chosen for antiproton selection :

$$n_{p.e} \leq 0.15 \ p.e \tag{8}$$

For this cut, the rejection is $R_{e^-} \simeq 330$ and the efficiency is up to $\epsilon_{\bar{p}} \simeq 48\%$, depending on the momentum (see fig. 15).

[3]The aerogel refractive index has been measured with a $\lambda = 570nm$ (red) diode

As a conclusion, it can be said that ATC provides a rejection of ~ 330 against e^-. This information may be combined with Tracker and TOF measurements to estimate $\bar{p}/p$ up to 2-2.5 GeV/c. Above this momentum, and up to 3.5 GeV/c, ATC might also extend the evaluation of $\bar{p}/p$.

3.4 e^+ selection with ATC

The ATC can also be used to discriminate e^+ from protons (the signal to background ratio is estimated to be $e^+/p \sim 10^{-3}$). Such a selection may be useful to enhance the redundancy on $e^+/(e^- + e^+)$ measurement.
Positrons are expected to deposit a large signal in each ATC layer. On the other hand protons below threshold will potentially contaminate the e^+ selection due to both residual signal of every cell (scintillation, δ-rays) and the PMT-window Čerenkov radiation. Furthermore these physical signals can be artificially stressed by after-pulses effects present on Hamamatsu PMT (see section 3.1).
Positrons can then be selected by requiring an aerogel path length greater than $8cm$/layer and a number of photo-electrons greater than 2 p.e/layer.
The efficiency so obtained is $\epsilon_{e+} \sim 45\%$ with a proton rejection up to $R_p \sim 150$.
The proton contamination coming from particles passing close to the PMT can be reduced with an appropriate cut on the impact parameter. Requiring the minimal impact parameter to be greater than 1.5 cm, one sets selection efficiency to $\epsilon_{e+} \sim 41$ % and proton rejection up to $R_p \sim 260$ (see fig. 16).
The proton rejection as a function of P(GeV/c) is shown on figure 16. It presents a decrease below 1 GeV/c, due to scintillation, and a decrease between 1 GeV/c and 3 GeV/c, due δ-rays (for more details, see 3.2.5).
It can be said that ATC provides a useful way of discriminating e^+ from p^+ background, in the 0.5-4 GeV/c range.

4 Conclusion

The general behaviour of the AMS apparatus during its first test flight on board of the space shuttle Discovery has been satisfactory. As far as the ATC is concerned, only one electronic channel was not working. Despite the aerogel ageing problem encountered, the ATC counter allowed to separate $\bar{p}$ and e^- with a rejection of 330 and efficiency up to $\sim 48\%$, extending the $\bar{p}/e^-$ separation range up to 3.5 GeV/c. As a secondary result, the ATC may also be used, with appropriate selections, to separate e^+ from proton background, with a rejection up to 260 and an efficiency $\epsilon_{e+} \simeq 41$ %.

References

[1] AMS Collaboration, *Search for Antihelium in Cosmic Rays*, Phys. Lett. **B461** (1999) 315

[2] E. Choumilov, *private communication*

[3] G.Barbielini *et al.*, Nucl. Instr. and Meth. **371** (1996) 164
Y.Asaoka *et al.*, Nucl. Instr. and Meth. **416** (1998) 236

[4] J.Alcaraz *et al.*, *The AMS Silicon Tracker: Performance Results from STS-91*, Contribution to ICRC (1999, Salt Lake City), session OG.4.2.02

[5] F.Barao, *Čerenkov detectors in AMS*, Proc. New Worlds in Astr. Physics (1998, Faro)
T.Thuillier *et al.* , *Prototype study of a proximity focusing RICH for the AMS experiment*, Proc. New dev. in photodetection (1999, Beaune)

[6] Hamamatsu Technical notes

[7] Matsushita Electric Works, Ltd 1048 Kadoma, Kadoma-shi, Osaka 571

[8] M.-H. A. Huang, *A geomagnetic Field Model for AMS Data Analysis*, AMS note.

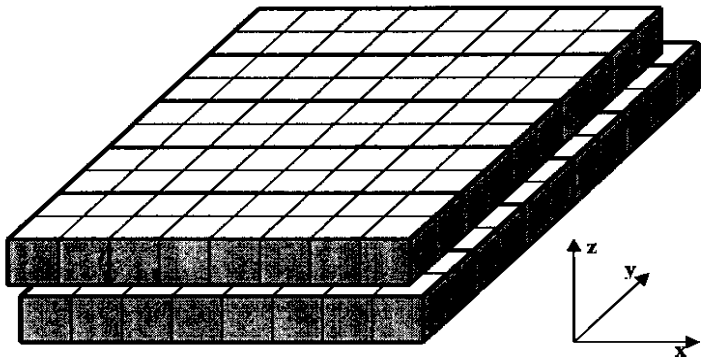

Figure 3: A diagrammatic view of ATC. The 2 shifted layers can be seen, containing respectively 80 and 88 cells.

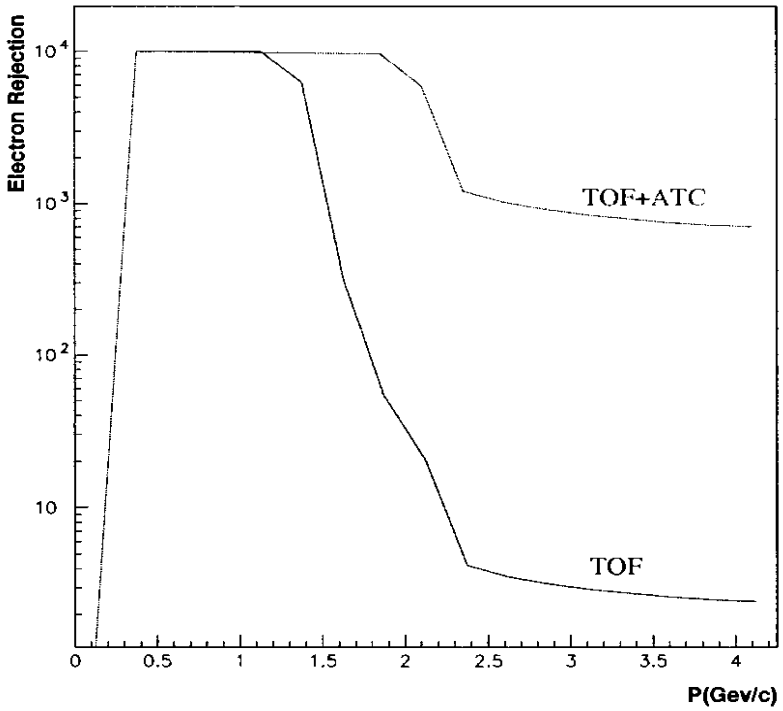

Figure 4: AMS Rejection. The upper figure shows rejection against electrons for TOF alone, as a function of P(GeV/c). It can been seen that above 1.5-2 GeV/c, the rejection is quit low, due to β resolution. The lower figure shows rejection against electrons for ATC and TOF. The improvement in the region from 1.5-2 GeV/c to 3.5 GeV/c can be seen. The figures have been obtained with a P resolution [4] $\Delta P/P = 7.\%$ and a β resolution [2] : $\Delta\beta/\beta = 3.3\%$ together with an ATC rejection $R_{ATC} = 300$.

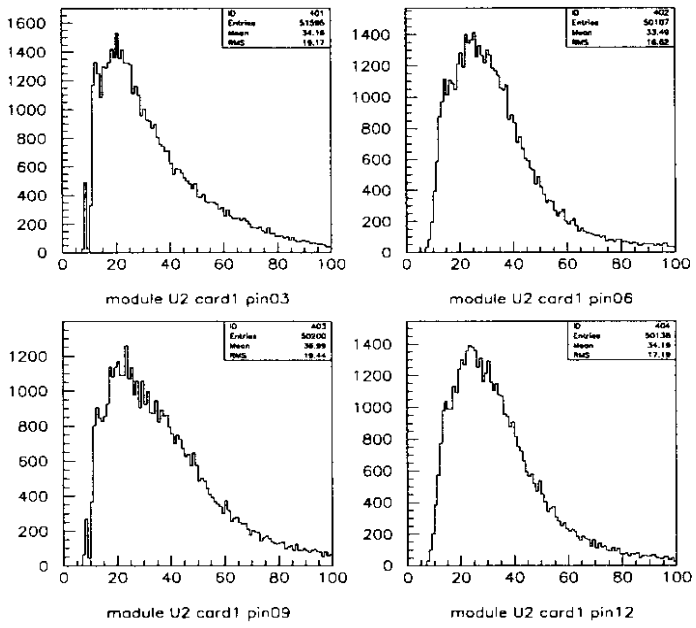

Figure 5: Four examples of single photo-electron distributions reconstructed from the Zurich calibration. One can see the effect of the electronics threshold.

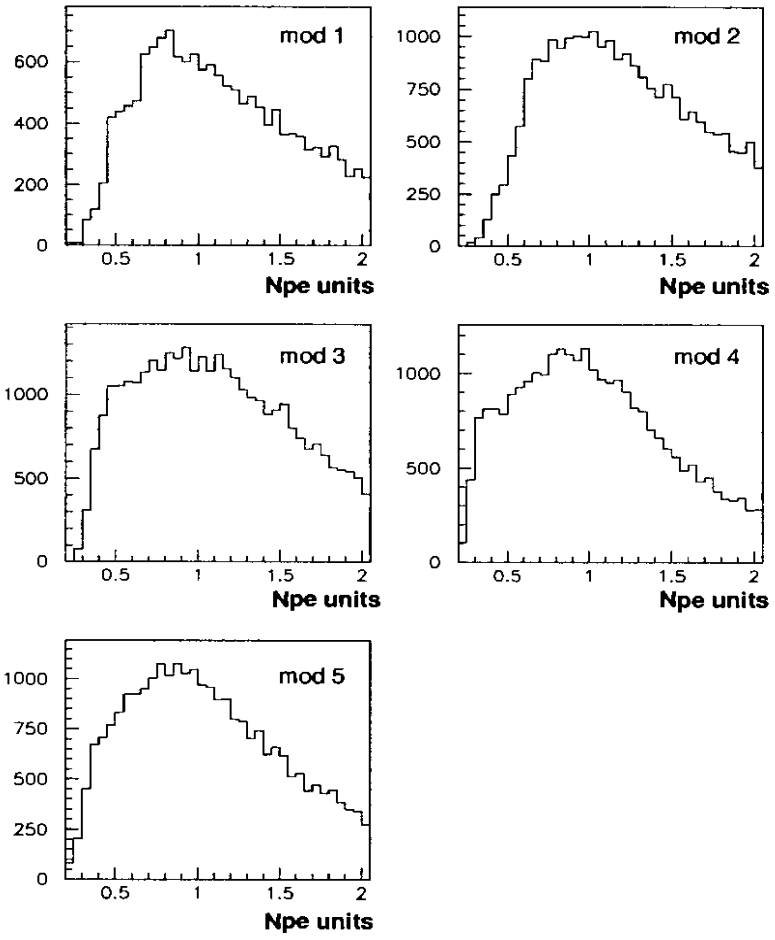

Figure 6: Below threshold proton distributions for the 5 modules of the first ATC layer.

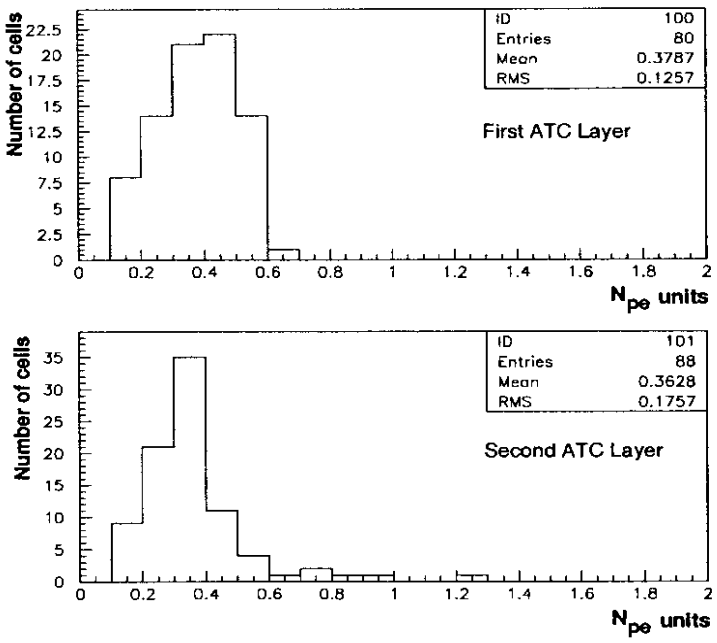

Figure 7: Distribution of the 168 thresholds in photo-electron unit, for the upper ATC plane and the lower one. It reflects the dispersion of the PMT gains.

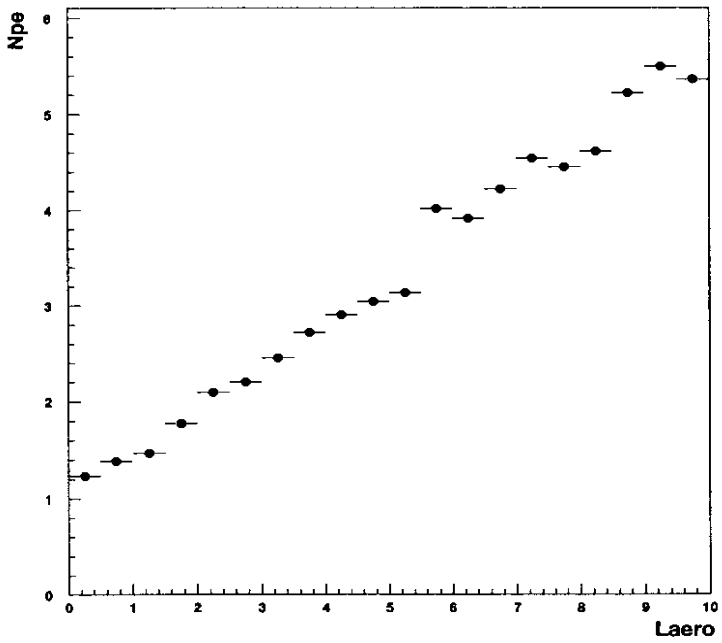

Figure 8: The cell luminosity shows a linear dependance with the aerogel pathlength.

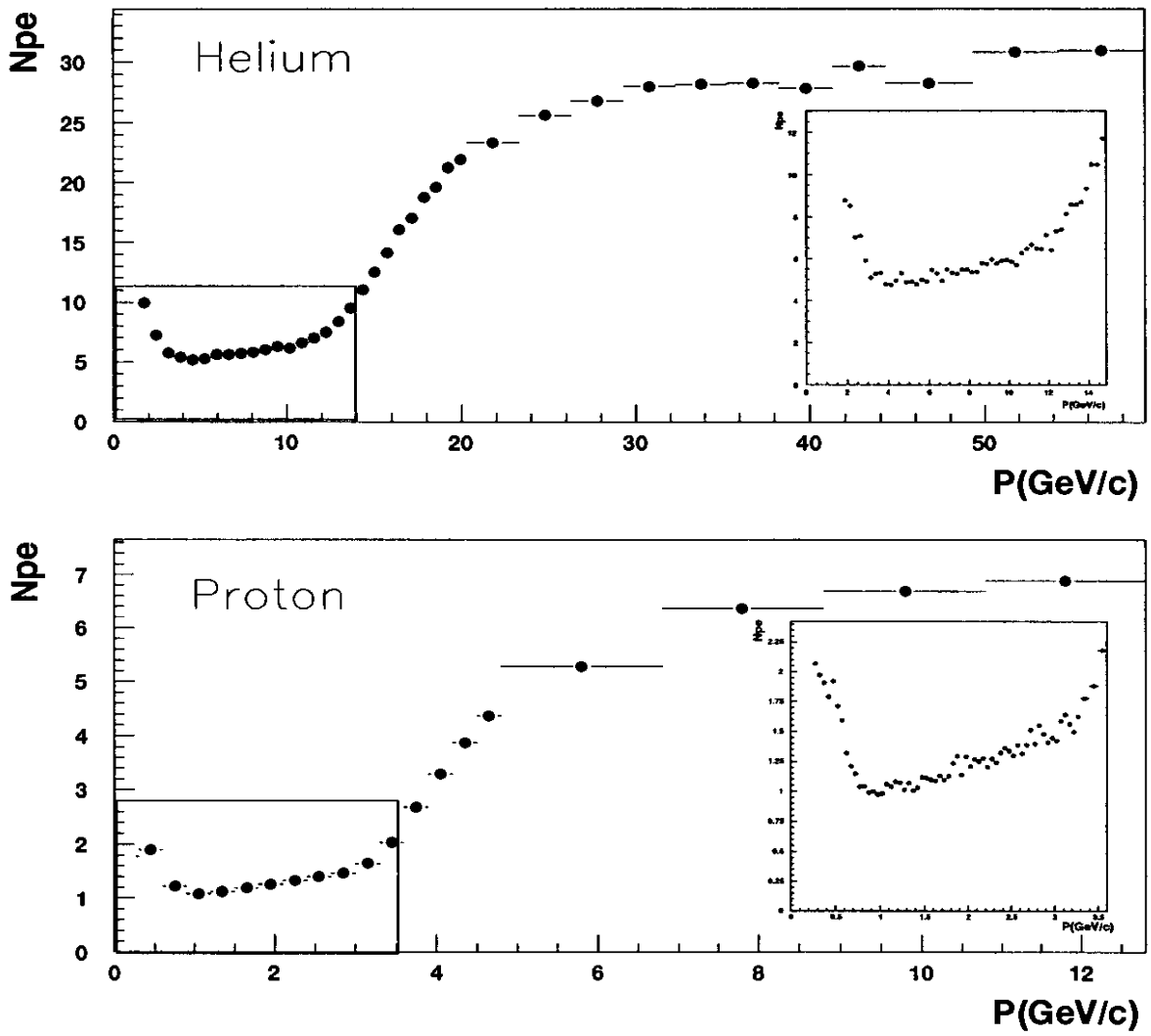

Figure 9: Helium and proton spectra. The upper (lower) figure shows $n_{p.e}$ vs P(GeV/c) for helium (proton). The light increase below 1 GeV/c (for protons), due to scintillation can be observed on the detailed view.

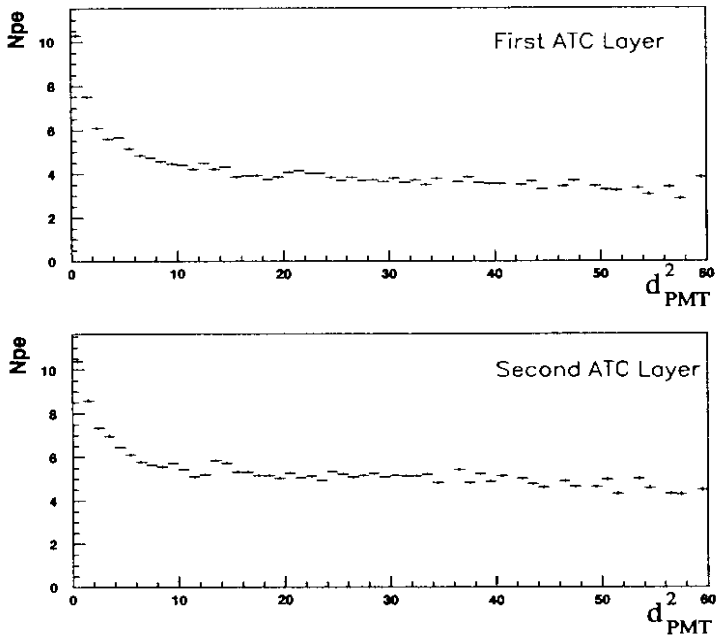

Figure 10: Distance to PMT. The upper (lower) figure shows $n_{p.e}$ as a function of the square of the impact parameter (d^2_{PMT}), for the first (second) ATC layer.

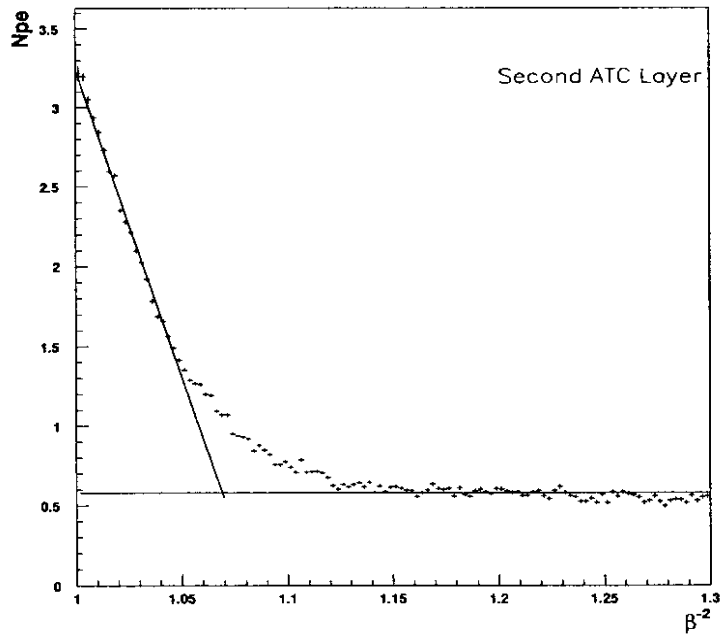

Figure 11: Refractive index evaluation. Number of photoelectrons ($n_{p.e}$), in the second ATC layer against $1/\beta^2$. For $1/\beta^2$ greater than 1.1 (corresponding to low momentum), the residual light can be observed, when $n_{p.e}$ reach a minimum. Below 1.1, $n_{p.e}$ is increasing with decreasing $1/\beta^2$. The extrapolation of the observed threshold leads to an evaluation of the refractive index.

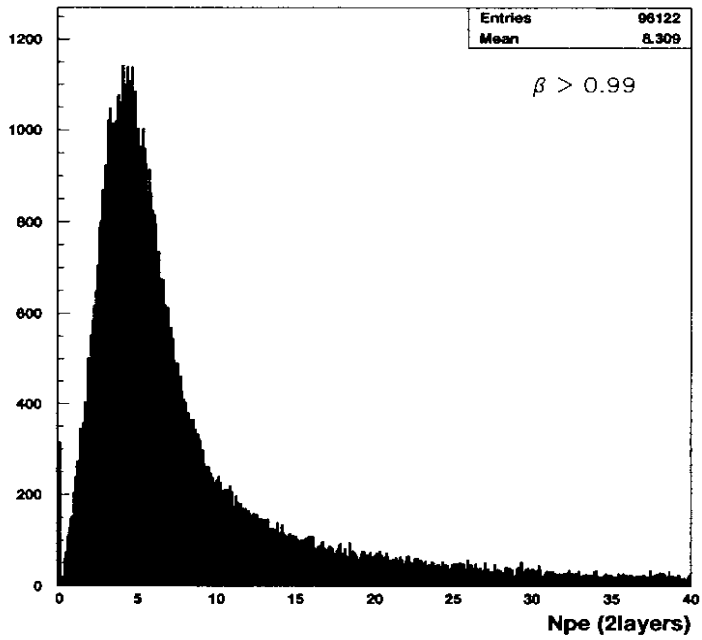

Figure 12: Above threshold signals in ATC. Distribution of $n_{p.e}$ for above threshold particles ($P \geq 15, \beta \geq 0.99$), selected near magnetic equator. This is similar to the behaviour of e^-, which are always above threshold. This sample is used to evaluate ATC rejection against electrons.

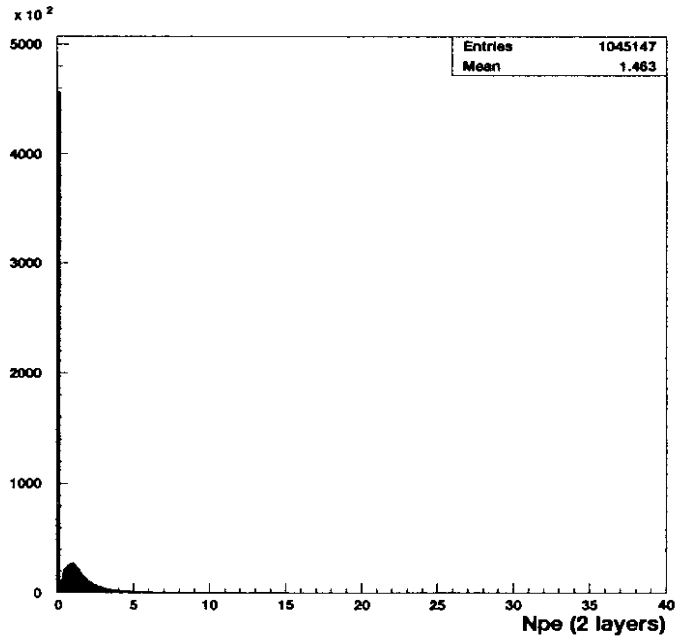

Figure 13: Below threshold signal in ATC. Distribution of $n_{p.e}$ for low energy protons ($P \leq 3.5$ GeV/c , $\beta \leq 0.97$ and $0.6 \leq M \leq 1.2$ GeV/c^2). Low energy $\bar{p}$ have the same behaviour in ATC.

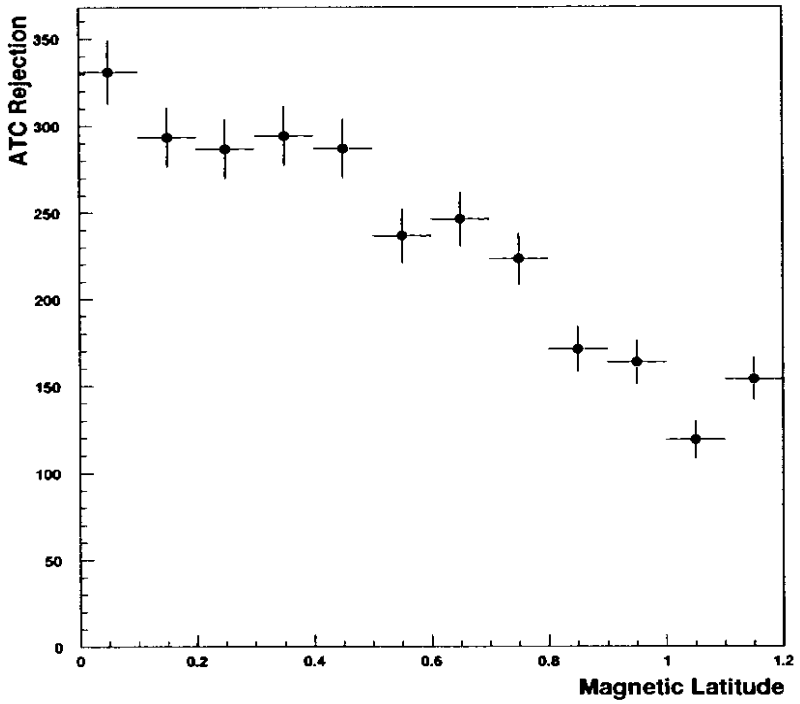

Figure 14: ATC Rejection ($n_{p.e} \leq 0.15$) against electrons as a function of magnetic latitude. The selected sample of $\beta = 1$ particles shows a higher purity for low magnetic latitude as there the rigidity cutoff is maximum.

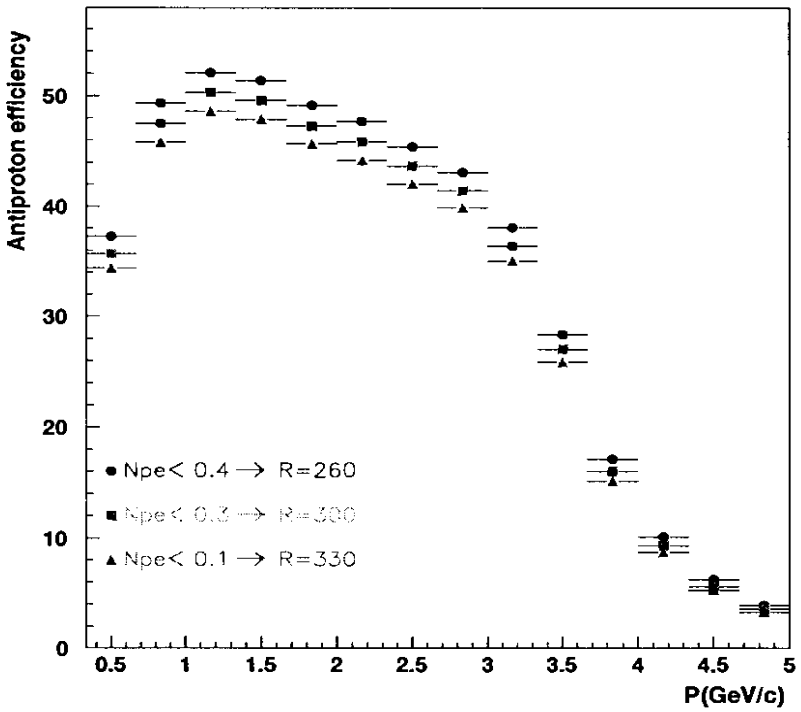

Figure 15: ATC selection efficiency for protons (antiprotons) as a function of momentum for different cuts on $n_{p.e}$. The electron rejection (R) is also indicated for each cut.

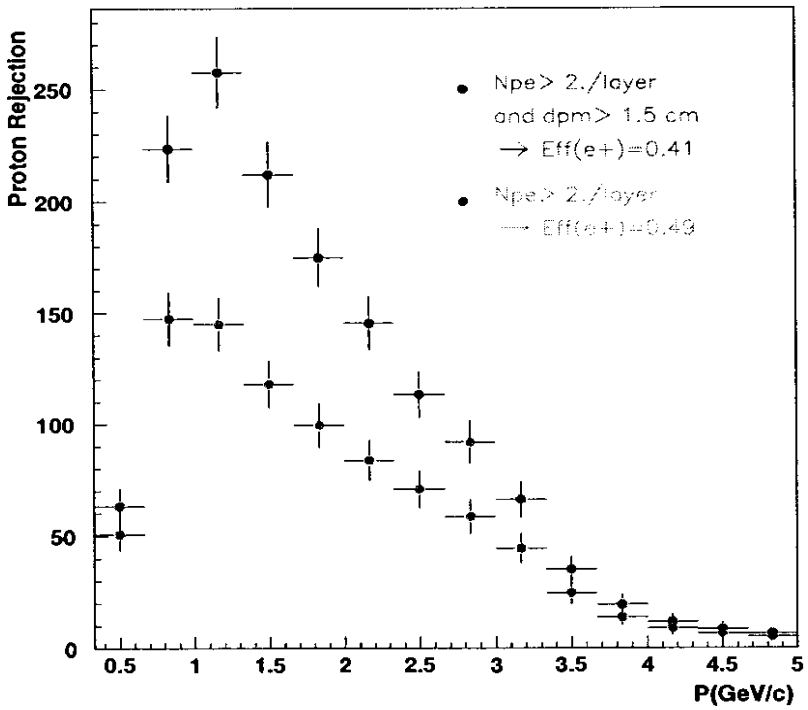

Figure 16: ATC positron selection : Proton rejection as a function of momentum for the 2 sets of selection. The positron efficiency (ϵ) is also indicated for each cut. It can been noticed that in both cases ATC proton rejection reaches a maximum near 1 GeV/c, where the ATC proton signal is at minimum.